Astronomy & Astrophysics

From Galaxy Clusters to Galaxy Dynamics: Predicting Extra Gravity from Baryonic Structure

Alejandro Rey⋆

Independent Researcher, Buenos Aires, Argentina

October 2026

ABSTRACT

Context. Gas pressure and weak gravitational lensing probe gravity in galaxy clusters in complementary ways. An energy-based response to baryonic structure connects the force balanced by gas pressure to the metric field that deflects light.
Aims. We test whether a response inferred from cluster gas support predicts hydrostatic masses, radial concentration and weak lensing in other clusters. Galaxy dynamics tests a complementary spatial response.
Methods. We calibrate one gas-density coefficient on 12 X-COP clusters and apply it to 46 LoCuSS clusters, including 18 with reduced-shear measurements. Weak lensing uses equal metric potentials, $\Phi = \Psi$. Controls comprise the basic local response, its constant amplification and a constant gas-fraction scaling; both scaling coefficients are calibrated on the same reference sample.
Results. Predicted hydrostatic masses have a mean absolute fractional error of about 20%, and the error in the concentration of additional mass at the intermediate aperture is about half that of the basic response. The gas-fraction control reaches similar mass accuracy, yet its lensing discrepancy is 2.4 times that of the density response, measured by squared errors weighted by the observational uncertainties. All three paired shear comparisons favour the density response after correction for multiple comparisons. A second prediction eliminates the calibrated density coefficient: measured gas support and gas-profile shape give lensing masses with an 11.0% mean absolute fractional error in eight clusters. In galaxies, the separately calibrated spatial response better predicts the radial structure of the gravitational residual inferred from rotation curves, using maximum-disk stellar masses.

Key words. galaxies: clusters: general – gravitational lensing: weak – gravitation – galaxies: kinematics and dynamics

1. Introduction

Gas pressure and gravitational lensing probe a cluster's gravity in complementary ways. The pressure gradient measures the inward force holding its hot gas in equilibrium; distorted background-galaxy images reveal how the cluster bends light. Both usually require much more gravitating mass than the observed baryons supply.

Temporal Inertia and Delayed Effects (TIDE) is a programme investigating how spacetime geometry responds to matter, including how it settles towards equilibrium (Rey 2026d). Here we calculate the additional gravitational field once equilibrium is reached. Its strength and spatial distribution follow from an energy model with baryons as the source. In clusters, gas density changes both the field that bends light and the force balanced by gas pressure. One coefficient, calibrated in reference clusters, stays fixed when predicting hydrostatic masses, radial concentration and weak-lensing shear elsewhere.

Earlier TIDE studies measured and predicted the radial decline of the gravitational residual in galaxies (Paper I; Rey 2026a) and its concentration in cluster hydrostatic profiles (Paper II; Rey 2026b). Paper IV examines delayed geometric response in merging clusters (Rey 2026c).

Galaxy rotation curves follow features in the luminous matter and a tight radial acceleration relation (Sancisi 2004; McGaugh et al. 2016). Modified Newtonian dynamics (MOND) describes a change in behaviour at low accelerations (Milgrom 1983); its aquadratic Lagrangian (AQUAL) formulation supplies a variational field theory (Bekenstein & Milgrom 1984). Refracted gravity introduces density dependence (Matsakos & Diaferio 2016) and has been tested with cluster galaxy kinematics (Pizzuti et al. 2025). Nonlocal gravity uses a spatial integral in the field equation (Rahvar & Mashhoon 2014), and Emergent Gravity motivates an additional response through an elastic analogy (Verlinde 2017).

X-COP hydrostatic profiles have tested hyperconical modified gravity (Monjo 2025). Joint X-ray and weak-lensing analyses have tested the distinct effects of modified gravity on gas support and light deflection (Sakstein et al. 2016). Emergent Gravity has been tested against galaxy weak lensing (Brouwer et al. 2017) and cluster baryonic and lensing mass profiles (ZuHone & Sims 2019; Halenka & Miller 2020). Resolved MOND modelling of the Bullet Cluster illustrates how compact galaxies and diffuse gas produce different lensing signatures (Hernandez 2026).

We compare the density response with the basic local law, constant amplification and constant gas-fraction scaling. Eliminating the density coefficient directly relates measured gas support and gas-profile shape to lensing mass. In disk galaxies, a separately calibrated spatial coupling controls the field's radial extent and is compared with local AQUAL.

Sections 2–4 present the data, equations and tests, with clusters first; Section 5 gives the conclusions. The appendices supply derivations and numerical details.

⋆ Corresponding author: rey.alejandro@usal.edu.ar. ORCID: 0009-0007-5052-3917.

2. Data

2.1. Cluster gas and hydrostatic masses

The XMM-Newton Cluster Outskirts Project (X-COP) provides gas-density, pressure and hydrostatic-mass profiles for the 12 calibration clusters (Ettori et al. 2019). Hydrostatic mass expresses the inward acceleration inferred from the pressure gradient as an equivalent enclosed mass. Calibration uses a fixed physical radius of 500 kpc, distinct from the overdensity radius r_{500}.

The Local Cluster Substructure Survey (LoCuSS) supplies a disjoint evaluation sample of 46 clusters (Martino et al. 2014), with 69 gas profiles from Chandra and XMM–Newton and 207 hydrostatic-mass measurements. Predictions are evaluated at the published r_{2500}, r_{1000} and r_{500}. These radii enclose mean densities of 2500, 1000 and 500 times the critical density of the Universe, respectively. Both catalogues use $H_0 = 70\ \mathrm{km\,s^{-1}\,Mpc^{-1}}$ and $\Omega_m = 0.3$.

Hydrostatic masses use the thermal-pressure gradient; turbulence and bulk gas motions can provide additional support. In the 21 LoCuSS clusters observed with both instruments, Martino et al. (2014) find $M_{\mathrm{Chandra}}/M_{\mathrm{XMM}} = 1.02 \pm 0.05$ at r_{500}, with about 8% intrinsic scatter. Their comparison with weak lensing is compatible with about 7% non-thermal pressure support at that radius.

2.2. Cluster weak lensing

Of the 46 LoCuSS evaluation clusters, 18 have gas coverage and at least three reduced-shear measurements between 500 and 1500 kpc, giving 74 radial bins. The profiles come from Okabe et al. (2010), except A2390, for which we use the contamination-corrected Euclid LensMC measurements of Schrabback et al. (2026). The sample comprises two disjoint groups of five and thirteen clusters, listed in Appendix C.4.

The relation between measured gas support and lensing mass is evaluated in eight LoCuSS clusters with gas and hydrostatic profiles covering the lensing R_{500} published by Herbonnet et al. (2020). These include the five-cluster shear group and none of the thirteen-cluster group. This comparison uses measured hydrostatic mass as an input to predict lensing mass; the direct shear prediction uses the gas profile and the calibrated response.

Five additional X-COP clusters have gas and hydrostatic profiles covering the apertures of Herbonnet et al. (2020); they test the relation without α outside the original eight objects. Six further LoCuSS clusters have gas coverage at the lensing R_{500} of Okabe & Smith (2016) and belong to neither the 18-cluster shear sample nor the eight-cluster mass sample. They test the calibrated density response. Appendix C.7 lists the objects and aperture conventions.

2.3. Galaxy observations

The Spitzer Photometry and Accurate Rotation Curves database (SPARC) provides stellar light, gas distributions and rotation curves (Lelli et al. 2016). The source and transition selection of Paper I (Rey 2026a) retains 124 galaxies with 1096 exterior velocity measurements: 82 galaxies and 730 points for calibration, and 42 galaxies and 366 points for evaluation. The stellar mass-to-light ratios use published maximum-disk values determined with rotation-curve information. Distances, inclinations and density reconstructions are retained. Appendix D specifies the radial selection and spatial calculation.

Galaxy lensing uses the isolated-galaxy GAMA and KiDS selections of Brouwer et al. (2021). GAMA (Galaxy And Mass Assembly) provides spectroscopic lens selection; KiDS (Kilo-Degree Survey) supplies imaging. We use the published lensing profiles, calibration corrections and full covariance, which includes correlations between radial measurements. Appendix D.2 specifies the selected bins and their overlap.

3. Methods

Figure 1 outlines the two applications.

3.1. An energy-based response to cluster gas

We write the weak-field potential as $\Phi = \Phi_b + \varphi$: Φ_b is produced by the baryons and φ is the proposed additional potential. Its spherical radial derivative, $q = \partial_r \varphi$, gives the magnitude of the additional inward acceleration. An energy functional assigns an energy to each possible field configuration. At equilibrium, small changes of the field leave that energy unchanged to first order. The local term W_0 sets the energy cost per unit volume of the additional response (Appendix A). In clusters, gas density changes this cost and therefore the field's strength and radial distribution:

$$W_{\mathrm{cl}}(q, \rho_g) = A W_0(q/A), \qquad A = 1 + \alpha \rho_g. \tag{1}$$

Here ρ_g is the local gas density and α sets its influence. The rescaling retains the basic response law, $\partial_q W_{\mathrm{cl}} = W_0'(q/A)$. The linear factor is the simplest density dependence with one global coefficient: it returns to W_0 at zero density and preserves convexity for $A > 0$ (Appendix B).

In this gas-source calculation, $g_{\mathrm{bar}} = GM_g(< r)/r^2$. Before density amplification, W_0 gives the spherical AQUAL acceleration excess

$$u(r) \equiv q_0(g_{\mathrm{bar}}) = \frac{2a_0}{1 + \sqrt{1 + 4a_0/g_{\mathrm{bar}}}}, \tag{2}$$

with $a_0 = 1.2 \times 10^{-10}\ \mathrm{m\,s^{-2}}$ throughout.

Varying the field at fixed gas density gives the metric response $q_{\mathrm{met}} = Au$: density multiplies the basic extra acceleration by A. Redistributing the gas also changes this energy and produces an additional force on the gas. Its coupling potential per unit mass is $\mu_c = \alpha[W_0(u) - uW_0'(u)]$.

In hydrostatic equilibrium (HSE), the pressure gradient measures the total acceleration needed to support the gas. Subtracting the baryonic acceleration defines the pressure-inferred excess, $q_{\mathrm{HSE}} \equiv -P'/\rho_g - g_{\mathrm{bar}}$, where P is gas pressure and primes on radial profiles denote d/dr. Pressure balance gives $q_{\mathrm{HSE}} = q_{\mathrm{met}} + \mu_c'$, including the density-coupling force. With mean enclosed density $\bar{\rho}_g = 3M_g/(4\pi r^3)$, the predictions are

$$\begin{aligned} q_{\mathrm{met}} &= (1 + \alpha\rho_g)u, \\ q_{\mathrm{HSE}} &= \left(1 + \frac{2}{3}\alpha\bar{\rho}_g\right)u, \\ M_{\mathrm{HSE,pred}} &= M_g + \frac{r^2 q_{\mathrm{HSE}}}{G}. \end{aligned} \tag{3}$$

The density amplification uses the local density for the metric field and the mean enclosed density for gas support.

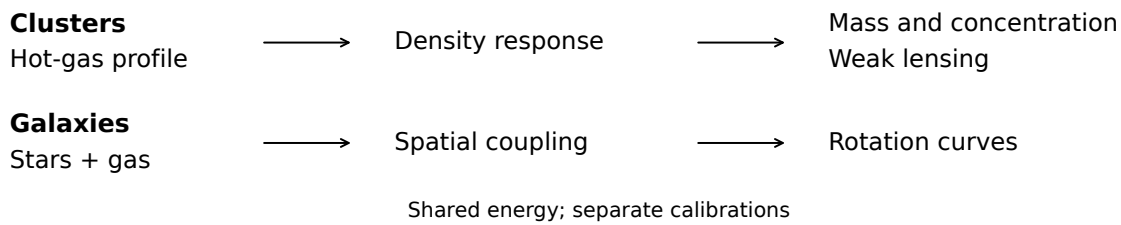


Fig. 1. Two applications of the local energy W_0. The cluster response relates gas support to the metric field used for lensing. Spatial coupling shapes galaxy rotation curves; galaxy lensing tests the local exterior response with full covariance.

3.2. From gas support to light deflection

The gas-response calculation determines Φ. The weak-field metric also contains a spatial-curvature potential, Ψ. Light deflection probes their mean, $\Phi_L = (\Phi + \Psi)/2$.

The local cluster energy admits a covariant formulation: one action determines both the metric field and the force on the gas. This construction uses a scalar field to define a preferred family of time slices, following Blanchet & Marsat (2011), and includes the gas density in the same energy law $AW_0(q/A)$. Photons couple directly to the metric. Appendix B derives the field and gas equations and their static weak-field limit.

In that limit, the spatial metric equations give $\Psi = \Phi$ at leading order. The additional stresses enter at higher order for the regular, nonrelativistic gas configurations considered here. The resulting optical potential is

$$\Phi_L = \Phi = \Psi = \Phi_b + \varphi, \qquad A_{\rm rel} = 1. \tag{4}$$

Gas pressure balances both the metric force and the density-coupling force, while light probes the metric alone. Gas support and light deflection can therefore indicate different effective accelerations even with $\Phi = \Psi$.

Projecting $g_{\rm bar} + q_{\rm met}$ along the line of sight gives convergence κ, which describes focusing, and tangential shear γ_t, which describes image stretching around the cluster centre. The measured reduced shear is $g_+ = \gamma_t/(1-\kappa)$ (Bartelmann & Maturi 2017). Appendix C.4 specifies the projection and source distances.

Reconstructions of the lensing potential from X-ray gas profiles provide a precedent for connecting these observables (Konrad et al. 2013). In Equation (3), the increments $q_{\rm met} - u$ and $q_{\rm HSE} - u$ share the coefficient α, which cancels when the responses are combined. Their relative weight is set by the measured gas-profile slope $s_g = d\ln M_g/d\ln r = 3\rho_g/\bar{\rho}_g$:

$$q_{\rm met} = \frac{s_g}{2} q_{\rm HSE} + \left(1 - \frac{s_g}{2}\right) u. \tag{5}$$

The shape of the gas profile thus determines how to convert the force inferred from gas pressure into the field that bends light, without using the calibrated density coefficient. With u fixed by the gas mass and a_0, the lensing mass is $M_L = M_g + r^2 q_{\rm met}/G$ at the measured aperture. Section 4.3 tests this relation against lensing masses.

3.3. Calibration and comparison responses

We determine α by minimising squared fractional hydrostatic-mass error at 500 kpc in the 12 X-COP clusters. The result is

$$\alpha = 7.60 \times 10^{-5}\ {\rm kpc}^3\,{\rm M}_\odot^{-1}. \tag{6}$$

A whole-cluster bootstrap of the 12 calibration objects gives a 95% percentile interval $[6.82, 8.80] \times 10^{-5}$ in the same units. This measures sample-composition uncertainty at the measured profiles (Appendix C.3).

Two controls retain the same basic response u: the unamplified W_0 case and a constant amplification Bu. Minimising the same X-COP mass-error objective gives $B = 3.07$.

We also calibrate the simple relation $M_{\rm HSE,pred} = M_g/f_g$ on those same 12 objects and with the same objective. The resulting constant gas fraction is $f_g = 0.1054$. This empirical control takes only the observed gas mass as its source and applies one global multiplier; its excess-mass concentration equals the enclosed gas-mass ratio. To predict its shear, we specify the metric closure $q_{\rm met} = q_{\rm HSE} = (f_g^{-1} - 1) g_{\rm bar}$, giving $g_L = g_{\rm bar}/f_g$. This control and the three energy-based responses use the same gas-profile continuation and projection, with reduced shear computed after projecting the field.

In galaxies, the energy adds a spatial-gradient term with length ℓ, coupling the response in neighbouring regions. Minimising mean per-galaxy velocity error over the candidate lengths $\ell = 0, 0.3, 1, 3, 10, 30$ kpc in the 82 calibration galaxies selects $\ell = 3$ kpc. The control $\ell = 0$ is the local AQUAL response. Appendix D describes the equations and source conventions.

3.4. Error measures and statistical comparisons

For masses, fractional error is the predicted minus observed mass divided by the observed mass. We report its mean absolute value and, where specified, its root-mean-square (RMS) value. RMS gives more weight to large discrepancies and is also used for radial-concentration errors. Error contributions are averaged over instruments and radii within each cluster before giving all clusters equal weight.

For cluster shear, the reference diagonal score Q treats radial measurement errors as uncorrelated: each prediction error is divided by its measured uncertainty, then squared and summed. We assess its sensitivity to radial correlations with 36 specified covariance matrices at fixed data, individual error bars and predictions. The scores compare discrepancies; absolute goodness-of-fit probabilities require the measured covariance. To compare mean errors across clusters, each object contributes its instrument-averaged score per radial bin. An exact two-sided sign-reversal test assumes independent clusters and symmetric paired differences under the null (Appendix C.5).

Holm correction accounts for the three shear-control comparisons. In these paired tests, p measures how unusual the observed advantage would be under that null. Bootstrap intervals resample whole clusters to estimate sampling variation; single-cluster omissions check individual influence (Appendix C.5).

The MOND/EG comparison forms a separate family of four contrasts: two alternatives, each tested on mass and shear. Holm correction covers these four jointly. The MOND/EG mass comparisons use Monte Carlo sign reversals; draw counts and implementation are given in Appendix C.6.

For the GAMA and KiDS galaxy profiles, the full covariance C includes correlations between bins. We use $Q = (d - m)^T C^{-1}(d-m)$, where d and m are the measured and predicted profiles. With fixed predictions and Gaussian measurement errors, the reported probability is $\Pr(\chi^2_N \geq Q)$ for N bins. It tests agreement with the observed profile under the quoted uncertainties, rather than improvement over a competing model (Appendix D.2).

3.5. Physical distinctions from MOND and Emergent Gravity

We compare three ways of connecting baryonic structure to gravity, using the same cluster gas profiles, mass apertures and shear measurements. All calculations use gas as the source, with no additional particle mass or object-specific adjustment.

For MOND's spherical simple function $\mu(x) = x/(1 + x)$, where x is total acceleration in units of a_0 (Famaey & Binney 2005), the additional acceleration is $q_{\rm MOND} = u$ from Equation (2). TIDE shares this local AQUAL limit; the MOND mass and shear predictions coincide with the basic W_0 control.

Emergent Gravity (EG) attributes the excess to an elastic response of spacetime associated with dark energy (Verlinde 2017). Its acceleration scale is tied to the expansion rate H_0. For a spherical extended source, the enclosed gas mass and its radial slope give (Verlinde 2017; Ettori et al. 2019)

$$q_{\rm EG} = \sqrt{\frac{cH_0}{6}\, g_{\rm bar}(1 + s_g)}, \qquad s_g = \frac{d\ln M_g}{d\ln r}. \tag{7}$$

Here $H_0 = 70\ {\rm km\,s^{-1}\,Mpc^{-1}}$, as in the input catalogues. Both alternatives predict hydrostatic mass as $M_g + r^2 q/G$ and use $g_L = g_{\rm bar} + q$ for lensing. MOND follows the common-potential prescription of Bekenstein (2004); EG uses the apparent-mass prescription of Brouwer et al. (2017). Gas reconstruction, projection and source distances are common to all three predictions.

TIDE instead distinguishes the force balanced by gas pressure from the metric field, linking them through the gas-profile shape. The tests below examine both the calibrated response and the coefficient-free relation in Equation (5).

4. Results

Response coefficients calibrated on reference samples remain fixed throughout evaluation; none is fitted per evaluation object or to lensing.

4.1. Cluster masses and radial concentration

Mass prediction test. Can the gas distribution predict the gravity required to support the gas? We apply the X-COP response to 46 LoCuSS clusters and compare predicted hydrostatic masses with measurements at three radii per profile. The basic W_0 response has no density amplification; constant B amplifies it uniformly. These controls separate density dependence from overall field strength.

The mean absolute fractional error is 19.8%, versus 51.6% for the basic response and 29.1% for constant amplification (Table 1). Density dependence lowers the error in 44 and 32 of the 46 clusters, respectively. Figure 2 shows the comparison object by object.

Table 1. Mass and concentration errors in 46 LoCuSS clusters.

Response	Mass error	C_{2500}	C_{1000}
Newtonian gas	87.91%	—	—
Basic W_0 / MOND	51.61%	0.17044	0.14362
Constant B	29.13%	0.17044	0.14362
Constant gas fraction	19.90%	0.09535	0.07280
EG	26.94%	0.14981	0.12164
Density	19.81%	0.12700	0.06957

Mass errors are mean absolute fractional errors, with equal cluster weights. Concentration columns report root-mean-square errors (RMSE); lower values mean closer predictions. MOND denotes the spherical simple-function AQUAL law; EG denotes spherical Emergent Gravity (Section 3.5).

Radial concentration test. To test where the additional gravity is concentrated, we compare the excess mass inside each inner radius with that inside the outer reference radius:

$$C_\Delta = \frac{M_{\rm HSE}(r_\Delta) - M_g(r_\Delta)}{M_{\rm HSE}(r_{500}) - M_g(r_{500})}, \qquad \Delta = 2500, 1000. \tag{8}$$

A larger C_Δ means a greater fraction of the excess lies near the centre. Measured and predicted masses use the same apertures.

Constant amplification of W_0 cancels from this ratio, whereas density dependence changes it. The density response reduces the C_{1000} RMSE by 51.6% and also improves C_{2500} (Table 1): it predicts radial structure as well as overall strength.

Comparison with MOND and Emergent Gravity. MOND/AQUAL coincides with the basic response above; its paired comparison gives $p_{\rm Holm} \simeq 4.0 \times 10^{-6}$ by Monte Carlo estimation. TIDE also improves on EG in 37 of 46 clusters, with a mean gain of 7.13 percentage points, a 95% cluster-bootstrap interval [3.95, 9.83] and $p_{\rm Holm} = 9.2 \times 10^{-5}$. Both concentration errors are smaller than those of either alternative (Table 1).

Gas-fraction control. The gas-fraction control gives a comparable mass error of 19.9%. The mean paired difference is 0.09 percentage points in TIDE's favour, with a 95% cluster-bootstrap interval $[-4.09, 4.45]$. Gas-fraction scaling gives the smaller C_{2500} error (0.095 versus 0.127), while TIDE gives the smaller C_{1000} error (0.070 versus 0.073). Lensing tests whether this similar mass accuracy extends to light deflection.

Robustness checks. We vary the measurement radius and omit individual calibration or evaluation clusters to check stability. Across all three radii, the mean paired gain over constant amplification is 9.32 percentage points, with a 95% cluster-bootstrap interval [4.93, 13.78]. At a common physical radius of 750 kpc, the density-response error is 15.5%, compared with 23.3% for constant amplification. Appendix C.2 reports the dependence on measurement radius. Recalibrating after omitting each X-COP cluster in turn changes the full LoCuSS mass error only to 19.64–20.00%. The advantage over the two W_0-based controls remains positive after every evaluation-cluster omission (Appendix C.3).

4.2. Light deflection: shear profiles and lensing masses

What is predicted and compared. The response calibrated on X-COP hydrostatic masses is held fixed to predict how LoCuSS clusters stretch background-galaxy images. We compare 74 radial

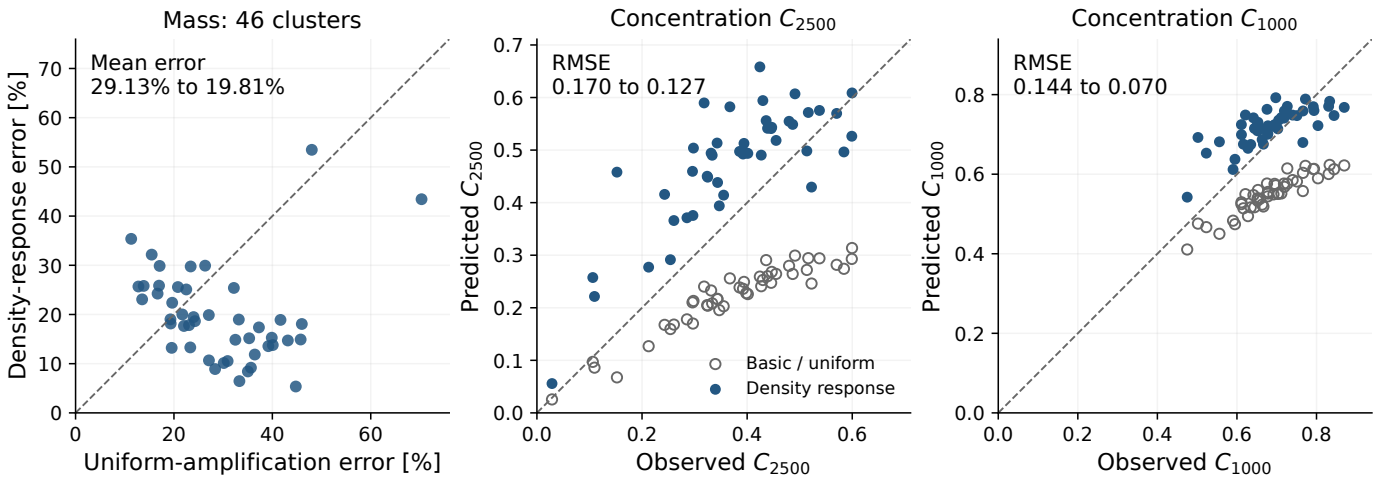


Fig. 2. Cluster mass and concentration predictions. Left: each cluster's mass error under constant amplification and density dependence; points below the diagonal favour the density response. Centre and right: predicted versus observed residual-mass fractions. Open symbols show the basic response, whose concentration is also that of constant amplification; filled symbols show the density response. All 46 clusters appear in each panel, with instruments averaged within objects. Dashed lines indicate equality.

Table 2. Shear scores and improvement over each control: 18 clusters, 74 bins.

Response	Q	TIDE gain	TIDE wins	p_{Holm}
TIDE (density)	86.94	—	—	—
Basic W_0	255.69	66.0%	16/18	9.2×10^{-5}
Constant B	194.06	55.2%	13/18	0.0305
Gas fraction	207.77	58.2%	14/18	0.0165

TIDE gain is the percentage reduction in Q relative to each control; wins count clusters with smaller errors. The two-sided paired test uses each cluster's score per radial bin. p_{Holm} accounts for all three contrasts; all models use $\Phi = \Psi$.

Table 3. Shear comparisons across 36 radial-correlation scenarios.

Comparator	TIDE lower Q	$p_{\mathrm{Holm}} < 0.05$
Basic W_0	36/36	33/36
Constant B	36/36	30/36
Gas fraction	36/36	30/36
MOND/AQUAL	36/36	33/36
EG	36/36	2/36

Counts refer to scenarios on the same 18 clusters, including the diagonal case. Holm correction follows Section 3.4 within each scenario. All matrices, individual results and verification scripts are included in the reproduction package.

measurements in 18 clusters with the density response and its three internal controls.

The result that separates the models. The density response and gas-fraction scaling have almost identical mean mass errors across the 46 clusters: 19.81% and 19.90%. In the 18-cluster lensing subset, the density response predicts shear more accurately in 14 objects and lowers the total shear score by 58.2%. The gas-fraction control equates the extra acceleration inferred from gas pressure with the additional metric field used to calculate lensing. TIDE's density-dependent energy distinguishes these two quantities and determines their relation.

Table 2 gives the scores and paired comparisons; Figure 3 shows the individual profiles.

Advantage under correlated radial errors. Could correlations between measurements at different radii erase the advantage? We recalculate the comparisons under 36 specified covariance scenarios, keeping the data, individual error bars and predictions fixed. The density response gives lower Q than every comparator throughout the grid. Even in the least favourable scenario, the reductions are 16.1% against constant amplification and 8.9% against gas-fraction scaling; each of these paired comparisons has $p_{\mathrm{Holm}} < 0.05$ in 30 of 36 scenarios (Table 3).

At the reference diagonal score, the 95% bootstrap intervals for mean gain lie above zero; all evaluation-cluster omissions and X-COP recalibrations also retain positive mean gains over the three internal controls. The package reports these stability checks in full.

Radial pattern of the errors. Constant amplification and gas-fraction scaling increasingly overpredict shear towards larger radii; the basic response underpredicts it. The density response has the smallest absolute mean residual in every radial band (Figure 4), between -0.32σ and $+0.05\sigma$. Here σ is the measurement uncertainty used to scale each error.

Comparison with MOND and Emergent Gravity. TIDE also has lower total discrepancy than EG (Table 4). MOND/AQUAL coincides with the basic response; its shear comparison remains significant after the joint mass–shear correction, with $p_{\mathrm{Holm}} = 9.2 \times 10^{-5}$.

Lensing masses in six additional clusters. We use the calibrated gas responses to predict lensing masses in six further LoCuSS clusters, comparing with Okabe & Smith (2016) at their lensing R_{500}. These objects belong to neither the shear sample nor the eight-cluster mass sample below.

The density response gives a mean absolute fractional error of 23.58%, the smallest among the four primary predictions (Table 5). Appendix C.7 reports RMS errors for all predictions.

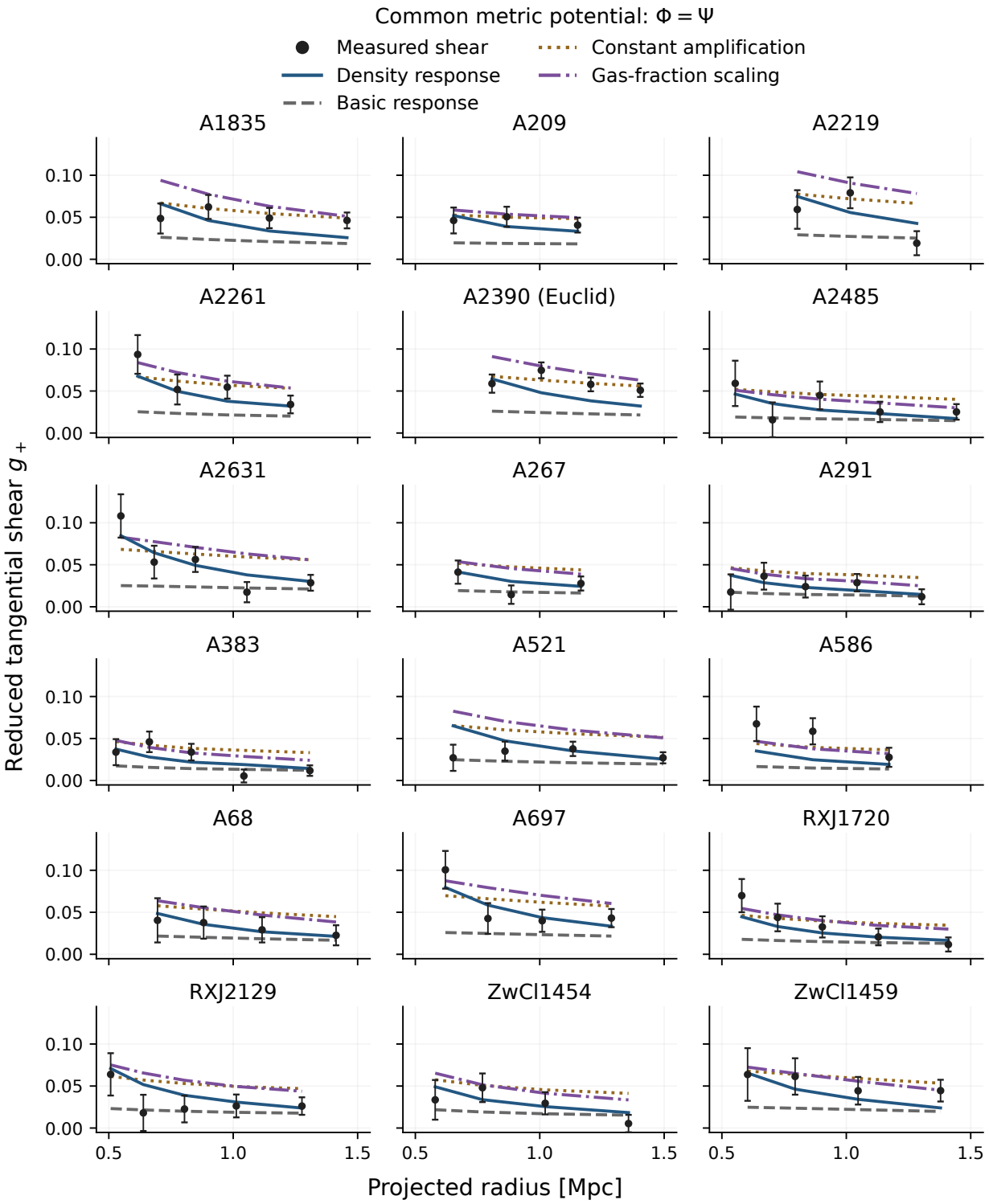


Fig. 3. Reduced-shear predictions for all 18 clusters and three internal controls, with $\Phi = \Psi$. Points show measurements over 500–1500 kpc; curves connect predictions at those radii. For two gas instruments, the curve averages their predictions; each prediction is scored separately before averaging the scores. A2390 uses Euclid LensMC; the other profiles are from Okabe et al. (2010). Axis scales are shared.

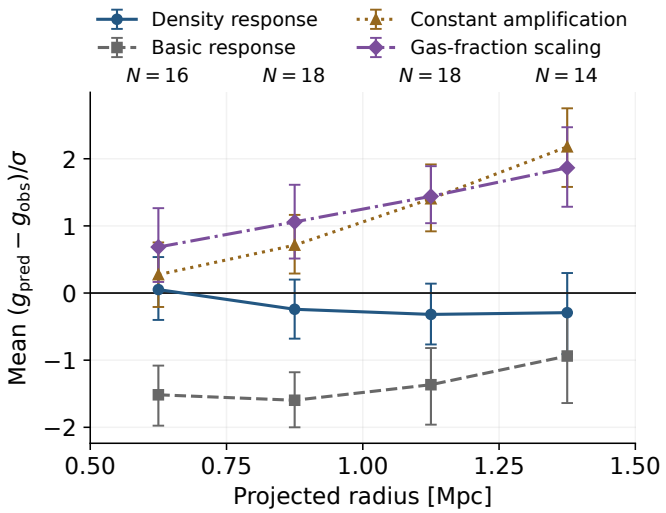


Fig. 4. Mean signed shear residual in four projected-radius bands. Zero means no average over- or underprediction; positive values indicate too much predicted shear and negative values too little. Individual errors can cancel in this average. After averaging instruments and radial measurements within each cluster and band, clusters receive equal weight; counts appear above the plot. Bars show pointwise 95% whole-cluster bootstrap intervals at fixed calibration and source profiles.

Table 4. Gravity-law predictions for the same 18 clusters.

Prediction	Q	TIDE wins	$p_{\rm Holm}$
TIDE	86.94	—	—
MOND/AQUAL	255.69	16/18	9.2×10^{-5}
EG	115.67	12/18	0.0525

Wins count clusters with lower loss for TIDE. Holm correction covers the two mass and two shear contrasts jointly. MOND and the basic W_0 control give the same predictions; their corrected probabilities refer to the two stated comparison families.

Table 5. Mean absolute fractional lensing-mass errors in six additional LoCuSS clusters. Lower values indicate closer agreement.

Prediction	Mean error	$p_{\rm Holm}$
Density response	23.58%	—
Basic W_0	34.62%	0.312
Constant B	70.02%	0.188
Gas fraction	49.26%	0.312

Probabilities compare cluster absolute errors with the density response, with Holm correction over the three controls. Nine instrument profiles contribute, with equal weight per cluster.

4.3. Predicting lensing mass without the density coefficient

Test of the gas–lensing relation. Can measured gas support predict lensing mass without the calibrated density coefficient? We apply Equation (5) to eight LoCuSS clusters using the measured hydrostatic residual $q_{\rm HSE}^{\rm obs} = G(M_{\rm HSE}^{\rm obs} - M_g)/r^2$ and gas-profile slope. Predictions retain fixed a_0 and are compared with measured lensing masses at the published lensing R_{500}.

The mean absolute fractional error is 10.96%, compared with 40.75% for the basic response and 18.84% when the gas-inferred and metric excesses are set equal (Table 6). The identity's RMS fractional error is 13.01%.

Transfer to five additional clusters. Applying the same relation to five additional X-COP clusters, with lensing masses from Herbonnet et al. (2020), gives a mean absolute fractional error of 31.10%, compared with 45.84% for the basic response. The identity improves on that response in all five objects and on a fixed midpoint between the basic and hydrostatic residuals in four. Table 6 compares all controls; the identity's RMS error is 32.60%.

Table 6. Mean absolute fractional lensing-mass errors in the original eight LoCuSS and five additional X-COP clusters. All predictions use $\Phi = \Psi$.

Prediction	LoCuSS (8)	X-COP (5)
Equation (5)	**10.96%**	**31.10%**
Basic W_0	40.75%	45.84%
Equal residuals	18.84%	20.28%
Fixed midpoint	—	32.07%

Equal residuals sets $q_{\rm met} = q_{\rm HSE}$. The midpoint control sets $q_{\rm met} = (q_{\rm HSE} + u)/2$ and is evaluated in the five-object extension.

Numerical and uncertainty checks. Log-linear instead of monotone-cubic interpolation gives mean errors of 9.91% in the original eight objects and 30.95% in the five-object extension. Using gas profiles with calibrated α gives 24.34% in the original eight; the identity instead uses measured hydrostatic support.

Propagating the published measurement errors at fixed apertures retains the X-COP advantage over the basic response in the radially correlated cases conditioned on increasing enclosed gas mass: the conditional 95% intervals for the mean-error reduction remain positive. The intervals for the difference between samples include zero, so these simulations do not resolve a change in accuracy between them. Adding sample-composition uncertainty by resampling whole clusters also makes the X-COP gain intervals include zero. Appendix C.7 specifies the error models.

4.4. Galaxy tests: radial structure, rotation and lensing

The spatial response adds a gradient term to the local AQUAL energy. Both responses use maximum-disk SPARC inputs: the largest stellar contributions allowed by the adopted rotation-curve models. With separately calibrated $\ell = 3$ kpc, we predict exterior speeds in 42 evaluation galaxies; 35 also support a radial-shape comparison.

Radial structure: how quickly does the field decline?

We compare the radial decline inferred from rotation curves with the spatial and local predictions. The transition radius $R_{\rm t}$ is the first outward crossing where the observed additional acceleration overtakes the Newtonian acceleration of stars and gas. Shape is measured by the logarithmic slope of $m(R) = q(R)/R$, the additional contribution to squared angular frequency. We divide each profile by its own value at $R_{\rm t}$ to compare how it changes with distance independently of its overall strength (Appendix D).

The mean absolute error (MAE) in radial slope falls from 0.549 for the local response to 0.382 with spatial coupling, a 30.3% reduction. Twenty-six of the 35 galaxies improve. The mean paired gain is 0.166, with a 95% bootstrap interval $[0.050, 0.289]$ and two-sided $p = 0.0038$.

Rotation speeds: comparing predicted and observed motion

We compare predicted speeds with 366 exterior measurements, retaining amplitude as well as shape. TIDE reduces the mean per-galaxy absolute error from 48.11 km s^{-1} for the Newtonian field of the same stars and gas to 14.81 km s^{-1}: a 69.2% reduction, improving all 42 galaxies ($p_{\rm Holm} = 9.09 \times 10^{-13}$). Local AQUAL gives 16.30 km s^{-1}, with $p_{\rm Holm} = 0.122$ for the spatial–local comparison (Table D.1; Fig. D.1). The comparison with Newtonian baryons measures the gain from the full response; the radial-shape test identifies the clearest additional benefit of spatial coupling over local AQUAL.

Complementary galaxy lensing with full covariance

We test the strength and radial shape of the GAMA and KiDS galaxy-lensing profiles of Brouwer et al. (2021), using the full published covariance to account for errors shared between radial bins. With equal metric potentials, the local TIDE prediction coincides with simple-function MOND/AQUAL. We compare this shared prediction with Newtonian gravity and EG using the same stars-and-cold-gas inputs. The seven bins with the highest baryonic accelerations form the primary comparison; all fifteen GAMA bins test the wider range (Appendix D.2).

The shared local response gives lower covariance-weighted discrepancy than EG and Newtonian baryons in both GAMA ranges and in KiDS (Table 7). It agrees with the full 15-bin GAMA profile under the published covariance; the seven-bin GAMA goodness-of-fit probability is 0.048, and KiDS retains a larger discrepancy. All absolute probabilities are given in Appendix D.2.

Table 7. Complementary galaxy-lensing comparisons with full covariance. Lower Q indicates closer agreement.

Sample (bins)	TIDE/MOND	Newton	EG
GAMA (7)	14.19	58.02	14.50
GAMA (15)	18.17	95.95	18.43
KiDS (7)	42.30	739.66	45.26

All predictions use the same stars and cold gas, with no fitted lensing coefficients. The GAMA ranges overlap, and GAMA and KiDS share lensing measurements; these rows are not independent tests.

5. Conclusions

TIDE connects gas support to light deflection through a common density-dependent energy, with equal metric potentials in the static local weak-field limit. Calibrated on 12 X-COP clusters, the response predicts hydrostatic masses in 46 LoCuSS clusters and shear in 18 of them, without fitting to lensing.

The density response and gas-fraction control both give mean hydrostatic-mass errors of about 20%, yet the density response gives a 58.2% lower quadratic shear score. Lensing thus distinguishes descriptions with comparable mass accuracy. All three paired control comparisons are significant after correction at the reference diagonal score; lower total scores persist across the 36 tested radial-correlation scenarios.

Equation (5) predicts lensing mass from measured hydrostatic support and gas-profile shape without the calibrated coefficient α. Mean absolute fractional errors are 10.96% in eight LoCuSS clusters and 31.10% in five additional X-COP clusters, below the basic response in both samples.

Using the same gas sources, TIDE predicts hydrostatic masses and radial concentration more accurately than simple-function MOND/AQUAL and spherical Emergent Gravity. Its total shear discrepancy is lower than either alternative, with significant improvement over MOND. In six additional LoCuSS clusters, the calibrated density response also gives the smallest mean absolute lensing-mass error among the four internal predictions.

In galaxies, spatial coupling improves radial shape under the maximum-disk source convention, while velocity predictions remain close to local AQUAL. In GAMA and KiDS lensing, the shared local TIDE/AQUAL response gives lower discrepancy under the full published covariance than EG and Newtonian baryons.

New gas and lensing profiles at matched radii directly test Equation (5): a systematic mismatch beyond measurement and modelling uncertainties would challenge the adopted gas–field coupling. Independent stellar-mass estimates would test the galaxy response under a different baryonic normalisation.

Data and code availability. Data and code are available on Zenodo: doi:10.5281/zenodo.23652311. The accompanying package contains this manuscript, inputs and reproduction scripts, with instructions in `README.txt`.

Acknowledgements. This work uses public rotation curves, baryonic mass models, X-ray profiles and gravitational-lensing measurements. The data teams are acknowledged in the references. OpenAI Codex was used for code development, verification support and manuscript preparation. The author is responsible for the scientific choices, interpretation and final text.

References

Bartelmann, M., & Maturi, M. 2017, *Scholarpedia*, 12, 32440, doi:10.4249/scholarpedia.32440.
Bekenstein, J., & Milgrom, M. 1984, *ApJ*, 286, 7, doi:10.1086/162570.
Bekenstein, J. D. 2004, *Phys. Rev. D*, 70, 083509, doi:10.1103/PhysRevD.70.083509.
Blanchet, L., & Marsat, S. 2011, *Phys. Rev. D*, 84, 044056, doi:10.1103/PhysRevD.84.044056.
Brouwer, M. M., Visser, M. R., Dvornik, A., et al. 2017, *MNRAS*, 466, 2547–2559, doi:10.1093/mnras/stw3192.
Brouwer, M. M., Oman, K. A., Valentijn, E. A., et al. 2021, *A&A*, 650, A113, doi:10.1051/0004-6361/202040108.
Brown, J. D. 1993, *Class. Quantum Grav.*, 10, 1579–1606, doi:10.1088/0264-9381/10/8/017.
Ettori, S., Ghirardini, V., Eckert, D., et al. 2019, *A&A*, 621, A39, doi:10.1051/0004-6361/201833323.
Famaey, B., & Binney, J. 2005, *MNRAS*, 363, 603, doi:10.1111/j.1365-2966.2005.09474.x.
Halenka, V., & Miller, C. J. 2020, *Phys. Rev. D*, 102, 084007, doi:10.1103/PhysRevD.102.084007.
Herbonnet, R., Sifón, C., Hoekstra, H., et al. 2020, *MNRAS*, 497, 4684–4703, doi:10.1093/mnras/staa2303, arXiv:1912.04414.
Hernandez, X. 2026, *ApJL*, 1008, L46, doi:10.3847/2041-8213/ae9d4c.
Konrad, S., Majer, C. L., Meyer, S., Sarli, E., & Bartelmann, M. 2013, *A&A*, 553, A118, doi:10.1051/0004-6361/201220663.
Lelli, F., McGaugh, S. S., & Schombert, J. M. 2016, *AJ*, 152, 157, arXiv:1606.09251.
Martino, R., Mazzotta, P., Bourdin, H., et al. 2014, *MNRAS*, 443, 2342–2360, doi:10.1093/mnras/stu1267.
Matsakos, T., & Diaferio, A. 2016, Dynamics of galaxies and clusters in refracted gravity, arXiv:1603.04943.
McGaugh, S. S., Lelli, F., & Schombert, J. M. 2016, *Phys. Rev. Lett.*, 117, 201101, arXiv:1609.05917.
Milgrom, M. 1983, *ApJ*, 270, 365–370.
Monjo, R. 2025, *ApJ*, 981, 195, doi:10.3847/1538-4357/adb723.
Okabe, N., Takada, M., Umetsu, K., Futamase, T., & Smith, G. P. 2010, *PASJ*, 62, 811–870, arXiv:0903.1103.
Okabe, N., & Smith, G. P. 2016, *MNRAS*, 461, 3794, doi:10.1093/mnras/stw1539, arXiv:1507.04493.
Pizzuti, L., Fantoccoli, F., Broccolato, V., Biviano, A., & Diaferio, A. 2025, *A&A*, 698, A83, doi:10.1051/0004-6361/202452739.

Rahvar, S., & Mashhoon, B. 2014, *Phys. Rev. D*, 89, 104011, doi:10.1103/PhysRevD.89.104011.
Rey, A. 2026a, Dark Halos Predicted from Baryonic Radial Transitions in Galaxies: Empirical Tests with SPARC and External Mass Models (Paper I), manuscript and reproducibility archive, doi:10.5281/zenodo.22664689.
Rey, A. 2026b, Dark Halos Predicted from Hydrostatic Structure in Galaxy Clusters: Empirical Tests with LoCuSS and X-COP Cluster Profiles (Paper II), revised manuscript, 13 October 2026. Earlier archive: doi:10.5281/zenodo.22853614.
Rey, A. 2026c, A Delayed Geometric Response in Cluster Mergers: Predictive Evidence from the Bullet Cluster and Abell 520 (Paper IV), manuscript and reproducibility archive, doi:10.5281/zenodo.23272604.
Rey, A. 2026d, Spacetime Has a Relaxation Time: A Constitutive Completion of Weak-Field Gravity, version 3.2, companion manuscript. Reproducibility archive: doi:10.5281/zenodo.21426036.
Sakstein, J., Wilcox, H., Bacon, D., Koyama, K., & Nichol, R. C. 2016, *JCAP*, 07, 019, doi:10.1088/1475-7516/2016/07/019.
Sancisi, R. 2004, in IAU Symposium 220, *Dark Matter in Galaxies*, ed. S. D. Ryder, D. J. Pisano, M. A. Walker, & K. C. Freeman, 233.
Schrabback, T., Congedo, G., Gavazzi, R., et al. 2026, *A&A*, 708, A345, doi:10.1051/0004-6361/202556310.
Verlinde, E. P. 2017, *SciPost Phys.*, 2, 016, doi:10.21468/SciPostPhys.2.3.016, arXiv:1611.02269.
ZuHone, J. A., & Sims, J. 2019, *ApJ*, 880, 145, doi:10.3847/1538-4357/ab2b34.

Appendix A: Constitutive law, spatial stiffness and field calculation

An auxiliary vector $\boldsymbol{p}$, with acceleration units and magnitude $p = |\boldsymbol{p}|$, represents the response. For a prescribed baryonic source, the galaxy energy is

$$\mathcal{F}[\Phi, \boldsymbol{p}; \rho_b] = \int \left[\frac{|\nabla\Phi - \boldsymbol{p}|^2 + \ell^2 \partial_i p_j \partial_i p_j}{8\pi G} + W_0(p) + \rho_b \Phi \right] d^3x. \tag{A.1}$$

The first squared term couples potential gradient and response; the gradient term penalises spatial variation. At equilibrium,

$$\nabla\cdot(\nabla\Phi - \boldsymbol{p}) = 4\pi G\rho_b, \qquad \nabla\Phi - \boldsymbol{p} = 4\pi G W_0'(p)\widehat{\boldsymbol{p}} - \ell^2\nabla^2\boldsymbol{p}. \tag{A.2}$$

Subtracting the baryonic Poisson equation gives $\nabla^2\varphi = \nabla\cdot\boldsymbol{p}$. In spherical symmetry $\boldsymbol{p} = q\widehat{\boldsymbol{r}}$; the galaxy calculation solves the fields in axial symmetry.

The local energy law is

$$W_0(s) = \frac{-s^2/2 - a_0 s - a_0^2 \ln(1 - s/a_0)}{4\pi G}. \tag{A.3}$$

For $0 \le s < a_0$, $W_0(0) = 0$ and $W_0'(s) = s^2/[4\pi G(a_0 - s)]$.

For $\ell = 0$, eliminating $\boldsymbol{p}$ gives

$$\boldsymbol{p} = \frac{a_0}{a_0 + g}\nabla\Phi, \qquad g = |\nabla\Phi|, \qquad \nabla\cdot\left[\frac{g}{a_0 + g}\nabla\Phi\right] = 4\pi G\rho_{\rm b}. \tag{A.4}$$

This gives the local AQUAL comparator with $\mu(x) = x/(1 + x)$ (Bekenstein & Milgrom 1984; Famaey & Binney 2005). For finite ℓ, the spherical boundary problem is

$$\frac{q^2}{a_0 - q} - \ell^2\left(q'' + \frac{2q'}{r} - \frac{2q}{r^2}\right) = g_{\rm bar}(r). \tag{A.5}$$

The final term accounts for the radial vector's changing direction.

At fixed source, let $\boldsymbol{v} = \delta\boldsymbol{p}$ and $\delta\Phi$ obey homogeneous Dirichlet conditions on a bounded domain. The potential constraint is

$$\nabla^2\delta\Phi = \nabla\cdot\boldsymbol{v}, \qquad \nabla\delta\Phi = \mathcal{P}_L\boldsymbol{v}, \qquad \mathcal{P}_L = \nabla\Delta_D^{-1}\nabla\cdot, \qquad \mathcal{P}_T = 1 - \mathcal{P}_L. \tag{A.6}$$

Here Δ_D^{-1} solves the potential boundary problem, while $\mathcal{P}_L$ and $\mathcal{P}_T$ project onto admissible gradient fields and their orthogonal complement. The reduced second variation is

$$\delta^2\mathcal{F}_{\rm red}[\boldsymbol{v}] = \int \left[v_i C^{ij}_{W_0} v_j + \frac{|\mathcal{P}_T\boldsymbol{v}|^2 + \ell^2|\nabla\boldsymbol{v}|^2}{4\pi G} \right] d^3x \ge 0. \tag{A.7}$$

The equilibrium Hessian $C^{ij}_{W_0} = \partial^2 W_0/\partial p_i \partial p_j$ has eigenvalues $W_0'(p)/p$ and $W_0''(p)$, positive for $0 < p < a_0$ and vanishing at $p = 0$. For $\ell > 0$, the boundary conditions exclude nonzero perturbations with zero cost.

The axisymmetric solver uses Φ, p_R, p_z, retaining p_R^2/R^2, with exponential disk thickness, spherical Abel-deprojected bulges and archived gas-ring reconstructions. Positive nodal quadrature for W_0 enforces $p < a_0$; a radial solution for the angularly averaged source sets the outer boundary. All 492 calibration and 84 evaluation solutions converge. Numerical checks include spherical solutions. Refining the production mesh and doubling the domain changes velocities by less than 0.6 km s^{-1} for the local control and 0.15 km s^{-1} at $\ell = 3$ kpc in the three control galaxies.

Appendix B: Covariant cluster energy, gas support and lensing

We derive the covariant field and gas equations, their static weak-field limit and Equation (5) in spherical gas equilibrium.

Appendix B.1: Action and constitutive choice

We use signature $(-+++)$ and coordinates $x^0 = ct$, retaining c explicitly. A scalar $\mathcal{T}$ defines a preferred time foliation, with future-directed unit normal n^μ. Following the construction of Blanchet & Marsat (2011), define

$$n_\mu = -N\nabla_\mu\mathcal{T}, \qquad N = (-g^{\mu\nu}\nabla_\mu\mathcal{T}\nabla_\nu\mathcal{T})^{-1/2}, \qquad h_{\mu\nu} = g_{\mu\nu} + n_\mu n_\nu, \qquad a_\mu = n^\nu\nabla_\nu n_\mu = D_\mu \ln N, \qquad a = (a_\mu a^\mu)^{1/2}. \tag{B.1}$$

Here D projects the covariant derivative into the time slices. The quantity a has inverse-length units; $c^2 a$ is the corresponding physical acceleration.

The gas is a relativistic perfect fluid with conserved rest-mass current and advected specific entropy, described by a fluid action S_g (Brown 1993). Its density is varied as a material variable:

$$J_g^\mu = \sqrt{-g}\,\rho_g u_g^\mu, \qquad \partial_\mu J_g^\mu = 0, \qquad u_g^\mu u_{g\mu} = -1, \qquad \rho_g = \frac{\sqrt{-g_{\mu\nu}J_g^\mu J_g^\nu}}{\sqrt{-g}}. \tag{B.2}$$

The fluid energy density is $\varepsilon_g = \rho_g c^2 + \varepsilon_{\rm int}$, including rest-mass energy. We vary $g_{\mu\nu}$, $\mathcal{T}$ and the fluid independently before selecting a static gas configuration.

For the local branch $\ell = 0$, take

$$S = \frac{c^3}{16\pi G}\int d^4x\,\sqrt{-g}[R - 2\Lambda - 2f(a,\rho_g)] + S_g + S_{\rm EM}. \quad \text{(B.3)}$$

$S_{\rm EM}$ is the minimally coupled electromagnetic action: photons follow the metric, with no direct coupling to the gas response. They are treated as probes of the cluster field. The local cosmological background represented by Λ is subtracted or negligible on the scales used below. The constitutive function is

$$f(a,\rho_g) = \frac{1}{c^4}\min_{0\le p<Aa_0}\Big[-2c^2ap + p^2 + 8\pi GAW_0(p/A)\Big], \qquad A = 1+\alpha\rho_g. \quad \text{(B.4)}$$

The auxiliary magnitude p retains the physical acceleration units of Appendix A, and W_0 is exactly Equation (A.3). Thus f has curvature units and the same a_0 and α specify the response. For the calibrated $\alpha \ge 0$, $A \ge 1$. The expression in brackets is strictly convex in p, since its second derivative is $2+8\pi GW_0''(p/A)/A > 0$. For $a > 0$, it has a unique stationary point inside the stated domain.

Writing $u = p/A$, stationarity and differentiation of the minimized function give

$$\begin{aligned} c^2a - p &= 4\pi GW_0'(u) = \frac{u^2}{a_0-u},\\ \chi &\equiv \frac{f_a}{2a} = -\frac{p}{c^2a},\\ \mu_c &\equiv \frac{c^4 f_{\rho_g}}{8\pi G} = \alpha[W_0(u) - uW_0'(u)]. \end{aligned} \quad \text{(B.5)}$$

The partial derivatives hold the other argument of f fixed. Terms containing derivatives of the stationary p vanish by its own field equation. At $a = 0$, the regular limit has $p = 0$. At $A = 1$, elimination also gives the explicit local function

$$f(a,0) = \frac{2a_0^2}{c^4}\left[\ln\left(1+\frac{c^2a}{a_0}\right) - \frac{c^2a}{a_0}\right]. \quad \text{(B.6)}$$

Appendix B.2: Metric and material variations

Keeping the densitized current J_g^μ fixed during metric variation gives

$$\delta\rho_g = \frac{\rho_g}{2}h^{(g)}_{\mu\nu}\delta g^{\mu\nu}, \qquad h^{(g)}_{\mu\nu} = g_{\mu\nu} + u_{g\mu}u_{g\nu}. \quad \text{(B.7)}$$

Consequently the density coupling contributes to the metric equation as well as to the gas force. Extending the metric variation of Blanchet & Marsat (2011) to $f(a,\rho_g)$ yields

$$G_{\mu\nu} + \Lambda g_{\mu\nu} + f g_{\mu\nu} + 2n_\mu n_\nu\nabla_\lambda(\chi a^\lambda) - 2\chi a_\mu a_\nu = \frac{8\pi G}{c^4}[T^{(g)}_{\mu\nu} + \rho_g\mu_c h^{(g)}_{\mu\nu}], \quad \text{(B.8)}$$

where $T^{(g)}_{\mu\nu} = (\varepsilon_g + P)u_{g\mu}u_{g\nu} + Pg_{\mu\nu}$. The added material stress $\rho_g\mu_c h^{(g)}_{\mu\nu}$ is isotropic in the gas rest frame. Derivatives of $\chi(a,\rho_g)$ in Equation (B.8) include density gradients.

Variation of $\mathcal{T}$ gives a further equation,

$$\begin{aligned} \nabla_\mu\mathcal{J}^\mu_{\mathcal{T}} &= 0,\\ \mathcal{J}^\mu_{\mathcal{T}} &= N\Big[n^\nu\nabla_\nu(\chi a^\mu) - \chi a^2 n^\mu - \chi(K^{\mu\nu} - h^{\mu\nu}K)a_\nu\Big], \end{aligned} \quad \text{(B.9)}$$

with $K_{\mu\nu} = h_\mu{}^\lambda\nabla_\lambda n_\nu$ and $K = K_\mu{}^\mu$. This form remains valid because $\rho_g(J_g, g)$ has no direct dependence on $\mathcal{T}$. In a static configuration aligned with $\mathcal{T} = x^0$, with zero shift and $u_g^\mu = n^\mu$, one has $K_{ij} = 0$ and $n^\nu\nabla_\nu(\chi a^\mu) = \chi a^2 n^\mu$. The current in Equation (B.9) then vanishes.

The independent fluid variation replaces its specific enthalpy $h_g = (\varepsilon_g + P)/\rho_g$ by $h_g + \mu_c$ in the material momentum. Using the Gibbs identity, including the advected-entropy term, gives the static force balance

$$D_iP + (\varepsilon_g + P + \rho_g\mu_c)D_i\ln N + \rho_g D_i\mu_c = 0. \quad \text{(B.10)}$$

For uniform specific entropy this also integrates to $N(h_g + \mu_c) =$ constant. Equation (B.10) itself allows a spatially varying entropy. With $N = 1 + \Phi/c^2 + O(c^{-4})$ and $P, \varepsilon_{\rm int}, \rho_g|\mu_c| \ll \rho_g c^2$, it reduces to

$$\nabla P + \rho_g\nabla(\Phi + \mu_c) = 0. \quad \text{(B.11)}$$

This derives the material force $-\nabla\mu_c$ used in the cluster predictions, with the material partial derivative evaluated as in Equation (B.5). Holding gas density fixed in both variations would omit this force and its metric stress.

Appendix B.3: Weak-field limit and the optical potential

Consider the regular static configurations just specified, in the weak-field metric

$$ds^2 = -\left(1+\frac{2\Phi}{c^2}\right)(dx^0)^2 + \left(1-\frac{2\Psi}{c^2}\right)\delta_{ij}dx^idx^j. \quad \text{(B.12)}$$

At leading order $a_i = \partial_i\Phi/c^2$. The constitutive law gives $0 \le p \le c^2a$. Since $W_0 \ge 0$ and $W_0(0) = 0$, its minimized function obeys $-a^2 \le f \le 0$. Convexity further gives $0 \le W_0(u) \le uW_0'(u)$, and hence

$$\frac{8\pi G}{c^4}\rho_g|\mu_c| \le \frac{2(1-A^{-1})p(c^2a-p)}{c^4} \le \frac{a^2}{2}. \quad \text{(B.13)}$$

Thus f, $\chi a_i a_j$ and the density-coupling stress are of order c^{-4} even when A is large. Pressure is also subleading under the nonrelativistic conditions above. In contrast, $\nabla_\lambda(\chi a^\lambda)$ contributes to the leading temporal equation, because χ can be of order unity.

The spatial metric equations at order c^{-2} are therefore

$$(\partial_i\partial_j - \delta_{ij}\nabla^2)(\Psi - \Phi) = 0. \quad \text{(B.14)}$$

Taking the trace gives $\nabla^2(\Psi - \Phi) = 0$. Regularity and matched boundary values for the two potentials remove the homogeneous solution, giving $\Psi = \Phi$ at this order. The temporal equation becomes

$$\nabla\cdot[(1+\chi)\nabla\Phi] = \nabla\cdot(\nabla\Phi - \boldsymbol{p}) = 4\pi G\rho_g, \quad \text{(B.15)}$$

where $\boldsymbol{p} = p\nabla\Phi/|\nabla\Phi|$ at this order. The combination $\chi\nabla\Phi = -\boldsymbol{p}$ has a regular zero-field limit. Together with Equation (B.5), these are the Euler equations of the static energy

$$\mathcal{F}_{\rm loc} = \int\left[\frac{|\nabla\Phi - \boldsymbol{p}|^2}{8\pi G} + AW_0(p/A) + \rho_g\Phi + \varepsilon_{\rm int}\right]d^3x, \quad \text{(B.16)}$$

with mass and entropy advected in the material variation. This is the cluster version of Equation (A.1), with active gas. For

minimally coupled light, the same metric gives $\Phi_L = (\Phi+\Psi)/2 = \Phi$ and the unit optical mapping of Equation (4).

The derivation covers the local static cluster branch. The galaxy rotation calculation retains the separate spatial-gradient term in Appendix A; its complementary lensing calculation uses the local exterior response. Adding minimally coupled stellar matter to the action would replace the source in Equation (B.15) by $\rho_g + \rho_\star$, while A would still depend only on ρ_g. The gas-only spherical identity below uses the source adopted in the cluster tests.

Appendix B.4: Spherical identity and radial concentration

For a regular spherical gas source, integrating Equation (B.15) gives $\partial_r\Phi - p = GM_g(<r)/r^2 = g_{\rm bar}$. Thus $p = q_{\rm met} = Au$, and stationarity gives $4\pi G W_0'(u) = g_{\rm bar}$, recovering Equation (2). At fixed α, the joint Hessian of $AW_0(p/A)$ in (p,ρ_g) is

$$\frac{W_0''(u)}{A}\begin{pmatrix} 1 & -\alpha u \\ -\alpha u & \alpha^2 u^2 \end{pmatrix} \geq 0. \tag{B.17}$$

Along the spherical equilibrium, the material coupling obeys

$$\begin{aligned} \mu_c' &= -\alpha u W_0''(u) u' = -\frac{\alpha u}{4\pi G} g_{\rm bar}', \\ g_{\rm bar}' &= 4\pi G\rho_g - \frac{2g_{\rm bar}}{r}. \end{aligned} \tag{B.18}$$

Primes on profiles denote d/dr. Equation (B.11) gives $q_{\rm HSE} = q_{\rm met} + \mu_c'$. Substituting cancels the local-density terms in the gas force:

$$\begin{aligned} q_{\rm HSE} &= \left(1 + \frac{2\alpha}{3}\bar\rho_g\right)u, \qquad \bar\rho_g = \frac{3M_g}{4\pi r^3}, \\ q_{\rm met} - u &= \alpha\rho_g u = \frac{s_g}{2}(q_{\rm HSE} - u), \qquad s_g = \frac{3\rho_g}{\bar\rho_g}. \end{aligned} \tag{B.19}$$

The second line recovers Equation (5) without dividing by α, and therefore includes $\alpha = 0$. For $\alpha > 0$ and positive density, the metric residual exceeds the hydrostatic one when $s_g > 2$, equals it at $s_g = 2$, and is smaller below.

For $M_{\rm res,HSE} = r^2 q_{\rm HSE}/G$, define $h(r) = \alpha M_g(r)/(2\pi r^3)$, $\gamma_g = 3 - d\ln M_g/d\ln r$, and $\beta_0 = (a_0 - u)/(2a_0 - u)$. The mean residual-density slope is

$$\gamma_{\rm HSE} \equiv -\frac{d\ln(M_{\rm res,HSE}/r^3)}{d\ln r} = 1 + (\gamma_g - 1)\beta_0 + \frac{\gamma_g h}{1+h}. \tag{B.20}$$

For $\gamma_g > 0$, the density-dependent term steepens the residual relative to W_0. For two fixed radii $r < R$, let $x = r/R$ and $C_g = M_g(r)/M_g(R)$ and $C_{\rm res} = M_{\rm res,HSE}(r)/M_{\rm res,HSE}(R)$. Then

$$\begin{aligned} C_{\rm res} &= x^2\frac{u(r)}{u(R)}\frac{1 + h(R)C_g/x^3}{1+h(R)}, \\ \left.\frac{\partial\ln C_{\rm res}}{\partial\ln C_g}\right|_{M_g(R),r,R} &= \beta_0(r) + \frac{h(r)}{1+h(r)} > 0. \end{aligned} \tag{B.21}$$

This positive derivative explains the concentration trend in Section 4.1.

Appendix C: Evaluation, projection and reproducibility checks

Appendix C.1: Galaxy velocity and shape estimators

At galaxy i's N_i exterior radii, let $d_{ik} = V_{{\rm pred},ik} - V_{{\rm obs},ik}$ and $e_i = N_i^{-1}\sum_k |d_{ik}|$. Both calibration and evaluation use $\bar e = N_{\rm gal}^{-1}\sum_i e_i$ (equal galaxy weights). Bootstrap samples retain each galaxy's radii together; paired Wilcoxon tests are two-sided. Velocity contrasts with Newtonian baryons and local AQUAL use Holm correction over the two controls. Velocity-gain intervals use 20,000 whole-galaxy bootstrap samples with seed 20261026.

For $m_{\rm mod} = \partial_R(\Phi - \Phi_b)/R$, the observed transition radius fixes both models' window. Linear interpolation at this radius sets each model's $m_{{\rm mod},t}$. With $x_k = \log_{10}(R_k/R_{\rm t})$,

$$\gamma_{\rm mod} = -\frac{\sum_k x_k \log_{10}[m_{\rm mod}(R_k)/m_{{\rm mod},t}]}{\sum_k x_k^2}. \tag{C.1}$$

The same estimator applies to the observed residual, with coverage criteria in Appendix D.

Appendix C.2: Cluster apertures and uncertainty propagation

We vary measurement radii and masses in the same 46 LoCuSS clusters (36 Chandra and 33 XMM–Newton profiles), with the weighting of Section 3.4. Paired intervals use 5,000 whole-cluster bootstrap draws (seed 20261019). Concentration ratios are calculated within each profile before averaging instruments.

Native-aperture predictions use the tabulated gas masses directly; the innermost radii r_{2500} span 210–710 kpc. Table C.1 compares native and fixed apertures. Fixed-aperture checks use log-linear mass interpolation within each profile's measured radial range. The intersection of all 69 ranges is 710–760 kpc; 750 kpc is the first 50-kpc grid point strictly above the largest inner radius. The 500/1000-kpc check retains 19 clusters covering both radii. Coefficients remain fixed.

At the fixed 500/1000-kpc pair, residual-concentration RMSE is 0.11802 for the density response and 0.14011 for W_0 or constant B. A coordinate sensitivity scaling all tabulated radii by 0.90–1.10 at fixed enclosed masses gives density-response mass errors of 19.12–20.97%. At the 0.90 scale, concentration RMSE is 0.17180 for the density response and 0.17139 for W_0.

For these 46 hydrostatic-mass predictions, uncertainty propagation uses 2,000 positive lognormal realisations per scenario, matching published mass means and standard deviations. Six scenarios combine latent radial correlations of 0 or 0.9 with gas–hydrostatic correlations of −0.5, 0 or 0.5. Instruments share perturbations within each cluster and aperture. With α and B fixed, these scenarios yield mean mass-error reductions of 9.85–13.18 percentage points over constant amplification, with central 95% intervals above zero in every scenario.

Appendix C.3: Calibration composition and individual-cluster influence

The α interval in Section 3.3 uses 100,000 X-COP resamples with replacement (seed 20261031), each minimising the original squared fractional-mass objective at 500 kpc. The endpoints are the 2.5th and 97.5th percentiles at fixed measured profiles.

For the constant-gas-fraction control, write $c_g = 1/f_g$ and $x_i = M_{g,i}/M_{{\rm HSE},i}$ in the same calibration sample. Minimising $\sum_i(c_g x_i - 1)^2$ gives $c_g = \max[1, \sum_i x_i/\sum_i x_i^2] = 9.48513$, or $f_g = 0.105428$. Its predictions use all 207 LoCuSS apertures and

Table C.1. Hydrostatic-mass errors at native and fixed physical apertures. The metric is the mean cluster absolute fractional error.

Apertures	Clusters	W_0	Constant B	Density response
r_{2500}	46	60.86%	14.01%	22.68%
r_{1000}	46	51.59%	23.52%	17.51%
r_{500}	46	42.39%	49.86%	19.25%
750 kpc	46	52.81%	23.27%	15.52%
500 and 1000 kpc	19	50.81%	28.66%	15.63%
Native radii, same subset	19	49.98%	31.11%	19.46%

the primary weighting; $C_\Delta = M_g(r_\Delta)/M_g(r_{500})$. The paired interval uses 100,000 whole-cluster resamples with the full-sample coefficients fixed.

Omitting each X-COP object and refitting the same objectives at 500 kpc on the other eleven gives $\alpha = (7.3505–7.9234) \times 10^{-5}$ kpc^3 M$_\odot^{-1}$, $B = 2.9982–3.1734$ and $f_g = 0.10363–0.10750$. Table C.2 gives mass and concentration ranges across these calibrations and minimum gains when an evaluation cluster is also omitted, using the recalibrated α and B. Appendix C.5 propagates all three recalibrations to shear.

Appendix C.4: From the metric field to reduced shear

With Φ_L given by Equation (4), the thin-lens potential for angular-diameter distances D_l, D_s, D_{ls} is

$$\psi(\boldsymbol{\theta}) = \frac{2D_{ls}}{c^2 D_l D_s} \int \Phi_{\rm L}(D_l\boldsymbol{\theta}, z)\, dz. \tag{C.2}$$

Convergence and shear follow from its second angular derivatives (Bartelmann & Maturi 2017). For the spherical lensing acceleration $g_L = GM_g/r^2 + q_{\rm met}$, define $\beta_s = D_{ls}/D_s$ and the physical deflection $\widehat{\alpha}$:

$$\begin{aligned}
\widehat{\alpha}(R) &= \frac{4R}{c^2}\int_R^\infty \frac{g_L(r)}{\sqrt{r^2-R^2}}\, dr,\\
\kappa_\infty(R) &= \frac{D_l}{2}\left(\frac{\widehat{\alpha}}{R} + \frac{d\widehat{\alpha}}{dR}\right),\\
\gamma_\infty(R) &= \frac{D_l}{2}\left(\frac{\widehat{\alpha}}{R} - \frac{d\widehat{\alpha}}{dR}\right),\\
g_+(R) &= \frac{\beta_s\gamma_\infty(R)}{1-\beta_s\kappa_\infty(R)}.
\end{aligned} \tag{C.3}$$

The subscript ∞ denotes unit source efficiency. For every model, the catalogue mean efficiency sets an effective source redshift in the source cosmology; its efficiency is then recalculated in the calibration cosmology.

Gas mass uses monotone cubic interpolation (PCHIP) in log mass and log radius, with $\rho_g = M_g(d\ln M_g/d\ln r)/(4\pi r^3)$. Beyond the last node, an r^{-4} density tail matches mass and density with finite total mass. The primary 500–1500 kpc interval keeps the derivative stencil above the first node. TIDE and the three controls share this interpolation and outer continuation.

The thirteen-cluster group contains A209, A2261, A2485, A2631, A267, A291, A383, A521, A586, RXJ1720, RXJ2129, ZwCl1454 and ZwCl1459. Its 161 recovered positive markers include 111 projectable bins, of which 55 satisfy the primary selection. Twenty-three lower error bars meet the source figure's display floor; the archived extraction uses their upper linear errors for the clipped side and records these cases. The remaining five clusters are A68, A697, A1835, A2219 and A2390, contributing 19 bins: 15 from Okabe et al. (2010) and four from Euclid.

A2390 uses four Euclid LensMC measurements at approximately 0.81, 1.01, 1.21 and 1.40 Mpc, extracted with error bars from Schrabback et al. (2026, Fig. 21), and the LoCuSS gas profile. Euclid uses $z_l = 0.228$, $H_0 = 70$ km s^{-1} Mpc^{-1} and $\Omega_m = 0.3$. Source efficiencies are 0.680 for LensMC, 0.676 for KSB+ and 0.680 for SE++. The latter two methods, evaluated separately, retain significant paired improvements over both W_0-based controls. Bounds from the published efficiency moments for positive mixtures of the eight source groups under mean-efficiency rescaling enter the source-efficiency sensitivity calculation.

All 74 retained measurements have symmetric errors σ. Total scores average over instruments before summing clusters; RMS uses the same weights.

Appendix C.5: Paired comparisons of cluster shear predictions

To compare mean shear errors, define the loss $L_{j,m} = Q_{j,m}/N_j$ from each cluster's instrument-averaged quadratic score and unique bin count. The paired gain is $d_j = L_{j,\rm control} - L_{j,\rm density}$. The exact two-sided probability is the fraction of all $2^{18} = 262144$ sign assignments with absolute sum at least $|\sum_j d_j|$. Grouping, null assumptions and Holm correction follow Section 3.4.

For the gas-fraction control of Section 3.3, projection multiplies gas-only convergence and shear by $1/f_g = 9.4851$ before forming reduced shear. Direct integrations for A209, A1835 and A2390 verify this step.

Figure 4 uses edges at 500, 750, 1000, 1250 and 1500 kpc. Signed standardised residuals are averaged over instruments, measurements within each cluster and band, then clusters equally. Pointwise 95% percentile intervals use 100,000 whole-cluster resamples (seed 20261031), retaining all models and bands jointly; the respective cluster counts are 16, 18, 18 and 14.

The recalibrations of Appendix C.3 propagate through the affine convergence and shear fields before recomputing reduced shear. Direct integrations at the coefficient extrema for A209 and A2390 verify this propagation. The reproduction package supplies recalibration ranges, separate-cohort comparisons, resampling intervals, individual-cluster omissions and covariance-sensitivity protocols and results.

Appendix C.6: Comparison with published gravity laws

The gravity-law comparisons use the projection of Appendix C.4, with $cH_0/6 = 1.13349 \times 10^{-10}$ m s^{-2} for EG.

Mass probabilities use 10^6 random sign assignments with a plus-one correction (minimum raw $p \simeq 10^{-6}$); shear uses exact enumeration as above. The four-contrast correction is specified in Section 3.4. Bootstrap intervals use 100,000 whole-cluster draws with recorded seeds. For mean shear gain over MOND and EG they are $[1.269, 3.869]$ and $[0.024, 0.732]$, respectively.

Table C.2. Mass and concentration stability under cluster omissions. The density-response range uses the full evaluation sample with each of the twelve X-COP calibration clusters omitted in turn. Minimum gains include an additional omission of each evaluation cluster.

Observable	Density-response range	Min. gain vs. W_0	Min. gain vs. B
Mass error (%)	19.64–20.00	31.38	6.82
C_{2500} RMSE	0.1225–0.1327	0.0323	0.0323
C_{1000} RMSE	0.0676–0.0722	0.0686	0.0686

Both α and B use the same eleven calibration objects in each fold. Gain is control error minus density-response error, in percentage points for mass and the tabulated units otherwise. These min–max ranges describe sample-composition sensitivity.

Log-linear interpolation preserves the mass-error and shear-score ordering. Analytic point-mass and power-law checks verify the EG force and projection; the TIDE calculation recovers the archived predictions, and independently combined optical fields recover the MOND shear.

Appendix C.7: Lensing-mass inputs

The mass comparisons in Section 4.3 use A68, A697, A1835, A1914, A2111, A2204, A2219 and A2390. Gas and hydrostatic masses are interpolated within their measured coverage to the published lensing R_{500} (Herbonnet et al. 2020).

The five-object extension uses A1795, A2029, A2142, A85 and ZW1215, separate from the original eight. X-COP enclosed gas masses and forward-method hydrostatic profiles (Ettori et al. 2019) are interpolated in log mass and log physical radius to the lensing apertures reported by Herbonnet et al. (2020). The gas interpolant's derivative supplies s_g; log-linear interpolation provides a numerical check.

The fixed-α comparison uses A1423, A2009, A2552, RXCJ1504.1−0248, ZwCl0857.9+2107 and ZwCl1021.0+0426. They are the six members of the 46-cluster mass sample with unambiguous matches to Okabe & Smith (2016), gas coverage at the lensing aperture, and no overlap with the 18 shear or eight identity objects. The nine eligible instrument profiles are evaluated without extrapolation. Published masses in $10^{14}h^{-1}M_\odot$ are converted with $h = 0.7$; R_{500} follows from $M_{500} = (4\pi/3)500\rho_{\rm crit}(z)R_{500}^3$. Both catalogues provide reconstructed lensing masses: Herbonnet's aperture deprojection and Okabe's mass fits use NFW profiles. RMS fractional errors are 30.01% for the density response, 36.55% for the basic W_0 response, 77.19% for constant amplification B, and 64.27% for constant gas-fraction scaling.

For each extension, absolute and squared fractional errors are averaged within each cluster before averaging clusters equally. All selected objects enter both metrics. Paired tests enumerate all 2^N sign reversals of the absolute-error differences; Holm correction covers the three controls within each extension. In the five-object identity comparison, $p_{\rm Holm} = 0.1875$ for each control. For $N = 5$, the minimum two-sided probability is $2/2^5 = 0.0625$, or 0.1875 after correction over three controls.

For the eight LoCuSS and five X-COP identity samples, we propagate the published gas, hydrostatic and lensing-mass errors with 50 000 Monte Carlo draws per case. Apertures and X-ray grid radii remain fixed. The gas mass, its slope s_g and u are recomputed together; all controls and instruments share each cluster's lensing-mass draw. The input tables supply marginal errors, so we evaluate 24 assumed radial, gas–hydrostatic and inter-instrument correlation scenarios. Radial errors are either uncorrelated, smoothly correlated over a radial scale, or coherent across the profile. We repeat each scenario with the additional condition that enclosed gas mass increases with radius, giving 48 cases in total.

Section 4.3 reports the conditional and whole-cluster uncertainty results. A1795 remains underpredicted in all smooth and coherent cases, with its individual 95% residual interval below zero. These intervals are conditional on the stated error models: the marginal lensing-mass errors are not a measured distribution at fixed R_{500}, and the joint profile covariance is unavailable. The reproduction files supply the full protocol, intervals, selection records, input hashes and numerical verification.

Appendix D: Galaxy calculation details

Appendix D.1: Source convention and radial selection

The observed residual and predicted circular speed are

$$q_{\rm obs}(R) = \frac{V_{\rm obs}^2(R) - V_{\rm bar}^2(R)}{R}, \qquad V_{\rm pred}^2(R) = R\,\partial_R\Phi(R,0). \quad \text{(D.1)}$$

Both models use the observed transition radius $R_{\rm t}$: the first upward crossing of $q_{\rm obs}/g_{\rm bar} = 1$, interpolated linearly between adjacent measurements.

The selected calibration gives a velocity MAE of 18.18 km s^{-1} (Section 3.3); radial shape is secondary. For $m(R) = q(R)/R$, the normalised decline is

$$\log[m(R)/m(R_{\rm t})] \simeq -\gamma \log(R/R_{\rm t}). \quad \text{(D.2)}$$

Smaller γ means a shallower q/R profile. Its contribution to squared circular speed is $Rq \propto R^{2-\gamma}$, flat for $\gamma = 2$. For an isolated finite baryonic mass, both responses approach $q \simeq \sqrt{GM_b a_0}/R$ at low exterior accelerations. Thus $m = q/R \propto R^{-2}$ recovers Paper I's $\gamma = 2$ limit.

Thirty-five galaxies have at least three exterior measurements; the other seven remain in the velocity test. Table D.1 defines the quality subset.

For the spatial response, the mean signed slope error is +0.091. Relative to local AQUAL, spatial coupling lowers velocity errors in 26 of 42 galaxies, with mean gain 1.49 km s^{-1} and a 95% galaxy-bootstrap interval [−1.29, 4.20] km s^{-1} (Figure D.1). Relative to the Newtonian field of the same baryons, the mean velocity-error reduction is 33.30 km s^{-1}, with a 95% galaxy-bootstrap interval [25.62, 41.12] km s^{-1}.

Appendix D.2: Galaxy-lensing profiles with full covariance

The GAMA and KiDS-bright excess surface-density profiles $\Delta\Sigma$ of Brouwer et al. (2021) use KiDS source shapes. The primary selection retains the seven highest-$g_{\rm bar}$ bins, zero-based indices 8–14, with published centres 1.2982×10^{-13}–3.9169×10^{-12} m s^{-2}. The 15-bin GAMA range check extends the lower centre to 1.3822×10^{-15} m s^{-2}.

Surface densities are supplied in $h_{70}\,M_\odot\,{\rm pc}^{-2}$; we use $h_{70} = H_0/(70\ {\rm km\,s^{-1}\,Mpc^{-1}}) = 1$. For the released multiplicative factors b_i, we apply $y_i = \Delta\Sigma_i^{\rm raw}/b_i$ and $C_{ij} = C_{ij}^{\rm raw}/(b_i b_j)$ once, select-

Table D.1. Galaxy prediction errors using the same stellar mass models (Section 2.3), with equal galaxy weights.

Quantity	Galaxies	Newtonian baryons only	Local AQUAL	Spatial TIDE	Paired p for TIDE vs. local	vs. Newtonian
Slope MAE	35	—	0.5485	0.3822	0.0038	—
Slope MAE, quality subset	15	—	0.3648	0.2846	0.073	—
Velocity MAE (km s^{-1})	42	48.11	16.30	14.81	0.122	9.09×10^{-13}

Probabilities use two-sided paired Wilcoxon tests: velocity contrasts include Holm correction over two controls; slope values are unadjusted. Newtonian baryons have no additional-field slope. The quality subset requires at least five exterior points and $R_{\max}/R_t \geq 2$.

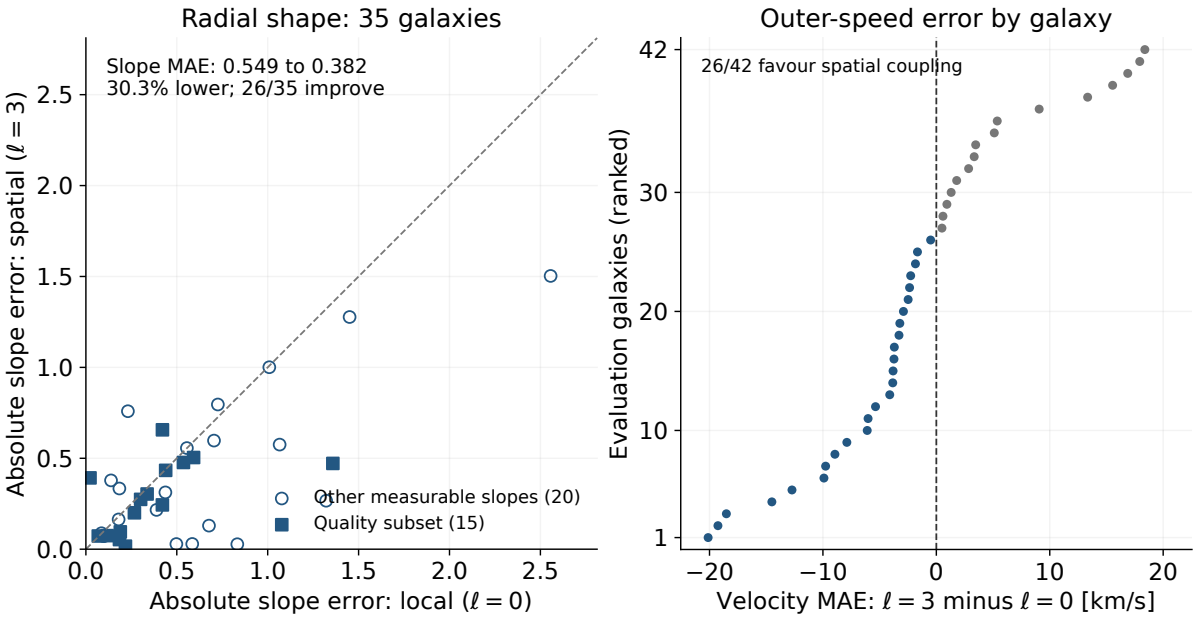


Fig. D.1. Galaxy predictions using the same baryonic inputs. Left: spatial versus local absolute slope errors for 35 profiles normalised at R_t; squares mark the 15-object quality subset. Right: spatial minus local velocity error for all 42 galaxies. Points below the left diagonal and negative right-panel values favour spatial coupling.

ing the covariance submatrix before inversion. This covariance excludes systematic uncertainties in the baryonic inputs.

The published stars-plus-cold-gas source is treated as a point mass, $g_{\rm bar}(R) = GM_b/R^2$. We project the local exterior response $q_0(g_{\rm bar})$ of Equation (2) along the line of sight to obtain $\Delta\Sigma_{q_0}$, giving

$$\Delta\Sigma_{\rm TIDE} = \frac{M_b}{\pi R^2} + \Delta\Sigma_{q_0}. \tag{D.3}$$

The Newtonian control retains the first term; simple-function MOND/AQUAL gives the same prediction as TIDE in this local calculation. Point-source EG gives $4G\Delta\Sigma_{\rm EG} = 4g_{\rm bar}/\pi + \sqrt{(cH_0/6)g_{\rm bar}}$. Baryonic inputs and published bin centres are common to all predictions; constants retain the values in Section 3.

For the common TIDE/MOND prediction, the absolute goodness-of-fit probabilities are 0.048 for the seven-bin GAMA comparison, 0.254 for all fifteen GAMA bins, and 4.6×10^{-7} for the seven-bin KiDS comparison.